SCIENTIFIC REPORTS

OPEN

Circuital characterisation of space-charge motion with a time-varying applied bias

Received: 11 November 2014
Accepted: 28 May 2015
Published: 02 July 2015

Chul Kim[1,3,*], Eun-Yi Moon[2,*], Jungho Hwang[1] & Hiki Hong[3]

Understanding the behaviour of space-charge between two electrodes is important for a number of applications. The Shockley-Ramo theorem and equivalent circuit models are useful for this; however, fundamental questions of the microscopic nature of the space-charge remain, including the meaning of capacitance and its evolution into a bulk property. Here we show that the microscopic details of the space-charge in terms of resistance and capacitance evolve in a parallel topology to give the macroscopic behaviour via a charge-based circuit or electric-field-based circuit. We describe two approaches to this problem, both of which are based on energy conservation: the energy-to-current transformation rule, and an energy-equivalence-based definition of capacitance. We identify a significant capacitive current due to the rate of change of the capacitance. Further analysis shows that Shockley-Ramo theorem does not apply with a time-varying applied bias, and an additional electric-field-based current is identified to describe the resulting motion of the space-charge. Our results and approach provide a facile platform for a comprehensive understanding of the behaviour of space-charge between electrodes.

An external current may be induced by the motion of space-charge between two electrodes. The Shockley-Ramo theorem[1,2] is widely acknowledged to provide a basic description of the external current. This theorem describes the current induced by a moving point space-charge between electrodes. It has a wide range of applications, including biological ion channels[3–5], solid-state devices[6–8], electrochemistry[9,10], electrical discharge[11,12], and semiconductor detectors[13–15]. The Shockley-Ramo theorem is useful for understanding the behaviour of point space-charges. For example, when this theorem is applied to calculate the gating current of an ion channel, it relates the microscopic motion of the ions to the macroscopic current recorded using a voltage clamp[3]. The Shockley-Ramo theorem does not, however, provide circuital information on the induced current. Although the motion of space-charge has aspects of resistance and capacitance, it provides only one combined current.

An equivalent circuit approach to understanding the space-charge behaviour may be more useful for investigation of dielectric barrier discharge[16–18]. Equivalent circuit models have been employed in nanopore sequencing[19–21] and nano-scale devices[22–24]. Such circuital studies predetermine the overall equivalent circuit, and the circuit components are typically evaluated experimentally. The resulting capacitance can be fixed[20,21] or time-varying[16–19]; however, the physical relationship between the space-charge and equivalent capacitance is not well understood. Nanopore studies have posed some basic and general questions, including the meaning of capacitance, and its evolution into the corresponding bulk properties[25].

Here we study the microscopic motion of discrete charges in circuital terms, and attempt to characterise the evolution thereof into macroscopic circuit components. One restriction in the derivation of the Shockley-Ramo theorem is the fixed applied voltage between the electrodes[1,2]. With our analysis,

[1]School of Mechanical Engineering, Yonsei University, Seoul 120-749, Republic of Korea. [2]Department of Bioscience and Biotechnology, Sejong University, Seoul 143-747, Republic of Korea. [3]Department of Mechanical Engineering, Kyung Hee University, Yongin 446-701, Republic of Korea. *These authors contributed equally to this work. Correspondence and requests for materials should be addressed to C.K. (email: kalsoo1@msn.com) or J.H. (email: hwangjh@yonsei.ac.kr)

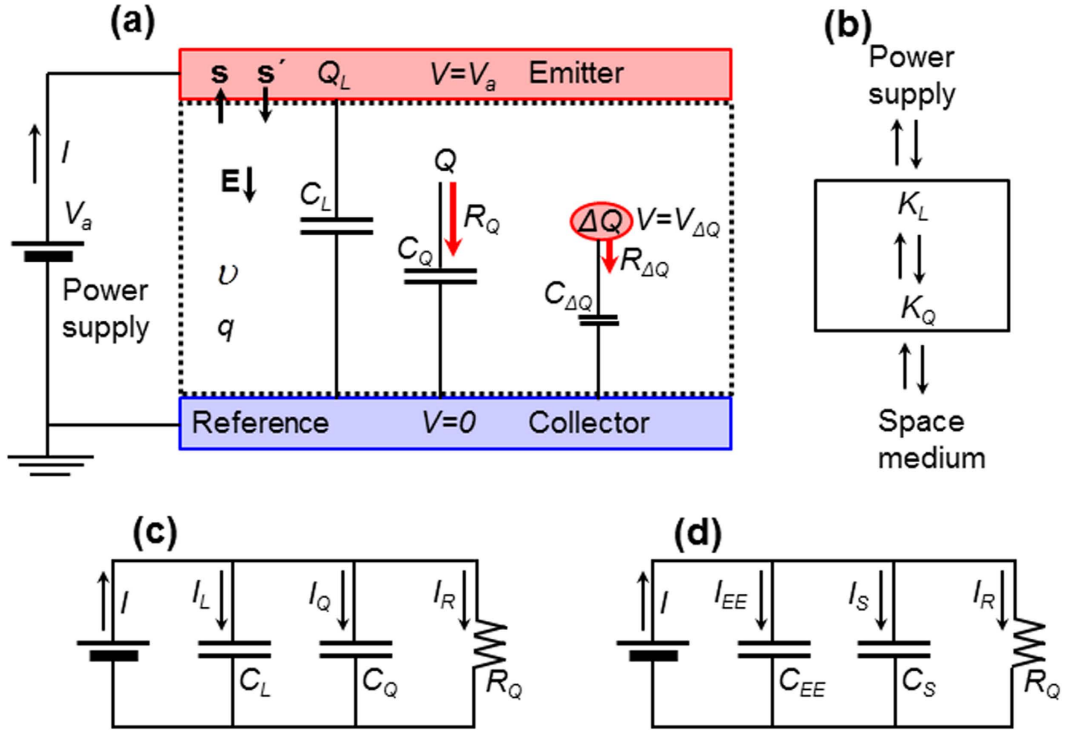

Figure 1. Schematic diagram of the two-electrode system and corresponding circuit diagrams. (**a**) The two-electrode configuration, where Q_L is charge on the electrode, $Q(=\int_\upsilon q d\upsilon)$ is the total space-charge, υ is the volume enclosed by dotted line, C_L is the capacitance between emitter and collector, C_Q is the equivalent capacitance of the charge Q, R_Q is the equivalent resistance of the charge Q, $C_{\Delta Q}$ is the equivalent capacitance of ΔQ, $R_{\Delta Q}$ is the equivalent resistance of ΔQ, $V_{\Delta Q}$ is the local electric potential imposed on ΔQ, **s** and **s′** are vector areas, and **E**↓ is the downward electric field. The downward field causes space-charge to drift downwards, as shown by the red downward arrows (↓). (**b**) A schematic diagram of the energy interactions. The rectangle shows the boundary of the system. (**c**) The equivalent electric circuit with charge-based current continuity. (**d**) The equivalent electric circuit with electric-field-based current continuity.

however, we consider a time-varying applied voltage for a simple system composed of only positive electrode-charge and positive space-charge. Our framework is based on conservation of the electrostatic potential energy of the system. This leads to two approaches: the energy-to-current transformation rule and the energy-equivalence-based definition of capacitance. Results obtained using this theoretical framework are validated via a comparison between experimental and numerical analyses of an air corona discharge with a time-varying applied voltage; i.e., a sinusoidally varying bias with a DC offset. Additional analyses are carried out to compare our results with those of the Shockley-Ramo theorem and the electric current that results from applying the Ampère-Maxwell equation. In particular, the time dependence of the capacitance due to space-charge is examined in detail.

Results

Framework. The proposed system consists of two electrodes separated by space, as shown in Fig. 1a. A positive electrode (the emitter) is connected to the positive terminal of a power supply, and the negative electrode (the collector) is grounded. The applied bias between the electrodes is V_a and the external current is I. The collector is set as a reference for the electric potential, so that the potential of the collector is zero and that of the emitter is V_a. The system consists of a positive electrode-charge Q_L and a positive space-charge Q. The electrostatic potential energy due to Q_L can be expressed as $K_L = 1/2 Q_L V_a$, and the electrostatic potential energy due to Q is given by $K_Q = 1/2 \int_\upsilon qV d\upsilon$, where υ is the volume between the electrodes, q is the charge density, and V is the electric potential with respect to the reference[26]. The quantity K_Q can be transformed in terms of the electric field using integration by parts after applying Gauss's law, and assuming that a constant permittivity ε[26]; i.e.,

$$K_Q = \frac{1}{2}\varepsilon \int_\upsilon E^2 d\upsilon + \frac{1}{2}\varepsilon \int_{Se} V_a \mathbf{E} \cdot d\mathbf{s} \tag{1}$$

where $E^2 = \mathbf{E} \cdot \mathbf{E}$, $\mathbf{E}(=-\nabla V)$ is the electric field, Se is the surface of the emitter, and **s** is the vector area (see Fig. 1a). The above relation can be written as $K_Q = K_{EE} + K_{VE}$, where $K_{EE} = 1/2\varepsilon \int_\upsilon E^2 d\upsilon$ and

$K_{VE} = 1/2\varepsilon \int_{Se} V_a \mathbf{E} \cdot d\mathbf{s}$. We use the symbol K to represent the charge-based electrostatic potential energy; i.e., K_L and K_Q, and we represent the electric-field-based electrical energy as K_{EE} and K_{VE}.

Figure 1b shows the total energy of the system. We use the same assumption as that used in the Shockley-Ramo theorem; i.e., that magnetic effects are negligible in the quasistatic regime[1,2]. The total electrical energy K_M in the system is then the sum of K_L and K_Q (i.e., $K_M = K_L + K_Q$). Consider the case whereby the power supply provides the system with an electric power $P(=IV_a)$ and there is no energy interaction with the space medium. Using conservation of energy, this input power will increase K_M to satisfy the relation $P = dK_M/dt = \dot{K}_M$. Therefore, if we know $\dot{K}_M$, the external circuit current can be expressed as $I = \dot{K}_M/V_a$. Based on this rationale, here we implement a streamlined energy-to-current transformation rule such that K_X (the electrical energy) $\rightarrow \dot{K}_X(=dK_X/dt$, the equivalent circuit power) $\rightarrow I_X(=\dot{K}_X/V_a$, the equivalent circuit current), where the subscript X represents a specific characteristic. Using this rule, we can conveniently transform the foregoing electrical energies to equivalent circuit currents for a given applied voltage such that $K_L \rightarrow \dot{K}_L \rightarrow I_L$, $K_Q \rightarrow \dot{K}_Q \rightarrow I_Q$, $K_{EE} \rightarrow \dot{K}_{EE} \rightarrow I_{EE}$, and $K_{VE} \rightarrow \dot{K}_{VE} \rightarrow I_{VE}$. In the same manner, energy relations are readily transformed to current relations such that $K_Q = K_{EE} + K_{VE} \rightarrow \dot{K}_Q = \dot{K}_{EE} + \dot{K}_{VE} \rightarrow I_Q = I_{EE} + I_{VE}$ and $K_M = K_L + K_Q \rightarrow \dot{K}_M = \dot{K}_L + \dot{K}_Q \rightarrow I_M = I_L + I_Q$.

The capacitance between the two electrodes is usually defined as $Q_L = C_L V_a$, where C_L is the capacitance of the electrodes (see Fig. 1a), and is the constant of proportionality between Q_L and V_a[26]. Here C_L is dependent only on the geometry of the system and the permittivity; $C_L = \varepsilon(A/d_g)$ for a pair of parallel electrodes, where A is the area of the electrodes and d_g is the separation between them. Here we assume that the electrodes are perfect electric conductors, so that the electric field inside the conductor is zero[26] and the electric potential of the electrode is equal to the applied bias. In addition, no external field can penetrate the conductor and the net induced charge is zero[26]. It follows that the electric field generated by the space-charge should not change the charge on the electrode Q_L, and that C_L is constant, even in the presence of space-charge. We define the capacitance using the following energy equivalence relation[26]:

$$K_L = \frac{1}{2} C_L {V_a}^2 \tag{2}$$

If we apply $K_L = 1/2 Q_L V_a$, the above expression reduces to $Q_L = C_L V_a$; however, equation (2) is of interest because our analysis is based on conservation of energy. For example, the capacitance due to the total space-charge (i.e., C_Q in Fig. 1a) is defined by $K_Q = 1/2 C_Q {V_a}^2$. Furthermore, this method can be extended to the electrical energy which does not include charge. The capacitance of the electrical energy stored in the electric field can be defined from $K_{EE} = 1/2 C_{EE} {V_a}^2$ [22]. Note that the above two definitions of capacitance result in different currents when the system is time varying. This will be discussed in greater detail later.

Discrete circuit components and evolution. As shown in Fig. 1a, a discrete positive charge ΔQ drifting between the two electrodes is assumed to have a discrete resistance $R_{\Delta Q}$. As ΔQ drifts due to the Coulomb force $\mathbf{F}_{\Delta Q}(=\Delta Q \mathbf{E})$, it does resistive Ohmic work due to ion-neutral collisions, where the work rate is $\mathbf{F}_{\Delta Q} \cdot \mathbf{U}_{\Delta Q}$[27]. Here $\mathbf{U}_{\Delta Q}(=\mu \mathbf{E})$ is the velocity of the discrete charge ΔQ and μ is the electrical mobility. In this way, the electrical energy of the system is converted into the thermal energy in the space between the electrodes[27]. The notation $\dot{K}_X$ can be used to describe the Ohmic work done by the charge ΔQ because this energy dissipation process consumes electrostatic potential energy. This microscopic process can be described by the discrete energy dissipation rate $\dot{K}_{\Delta R}$, which satisfies the energy equivalence relation $\mathbf{F}_{\Delta Q} \cdot \mathbf{U}_{\Delta Q} = \dot{K}_{\Delta R} = I_{\Delta R} V_a$, where $I_{\Delta R}$ is the equivalent discrete circuit current of $R_{\Delta Q}$. From this relation and using Ohm's law (i.e., $V_a = I_{\Delta R} R_{\Delta Q}$), we find that the discrete circuit resistance $R_{\Delta Q}$ is given by

$$R_{\Delta Q} = \frac{{V_a}^2}{\mathbf{F}_{\Delta Q} \cdot \mathbf{U}_{\Delta Q}}. \tag{3}$$

The total Ohmic work rate $\dot{K}_R(=\int_v \mathbf{F} \cdot \mathbf{U} dv$, $\mathbf{F} = q\mathbf{E}$, $\mathbf{U} = \mu \mathbf{E})$[27] in the space between the electrodes and the corresponding circuit resistance R_Q (see Fig. 1a) should satisfy the power relation $\dot{K}_R = I_R V_a$ as well as Ohm's law $V_a = I_R R_Q$, where I_R is the equivalent circuit current of R_Q. Using conservation of energy, the total $\dot{K}_R$ $(={V_a}^2/R_Q)$ is the sum of each discrete $\dot{K}_{\Delta R}$ $(={V_a}^2/R_{\Delta Q}$, see equation (3)), which leads to the relation $1/R_Q = \sum 1/R_{\Delta Q}$. Therefore, all of the discrete resistances can be said to evolve in parallel into the equivalent circuit resistance.

Note that ΔQ is assumed to have a discrete capacitance $C_{\Delta Q}$, as shown in Fig. 1a. Because the charge ΔQ leads to a local electric potential $V_{\Delta Q}$, the electrostatic potential energy due to ΔQ can be expressed as $K_{\Delta Q} = 1/2 \Delta Q V_{\Delta Q}$. From equation (2), we may write $K_{\Delta Q} = 1/2 C_{\Delta Q} {V_a}^2$ to define $C_{\Delta Q}$ as the equivalent discrete circuit capacitance due to ΔQ. From those two expressions, we may write $C_{\Delta Q}$ as follows:

$$C_{\Delta Q} = \frac{\Delta Q V_{\Delta Q}}{{V_a}^2}. \tag{4}$$

From conservation of energy, the total energy $K_Q(=1/2C_Q{V_a}^2)$ is the sum of each discrete term $K_{\Delta Q}(=1/2C_{\Delta Q}{V_a}^2)$, which leads to $C_Q = \sum C_{\Delta Q}$. Hence, all of the discrete capacitances can also be said to evolve into the equivalent circuit capacitance in a parallel topology.

Development of the charge-based circuit. The overall instantaneous application of conservation of energy for the system leads to $V_a I - \dot{K}_R = \dot{K}_M$, where $V_a I$ is the input power from the power supply, $\dot{K}_R$ is the power loss from the system to the space medium, and $\dot{K}_M(=\dot{K}_L + \dot{K}_Q)$ is the rate of change of the total electrostatic potential energy inside the system. This in turn leads to $I = \dot{K}_L/V_a + \dot{K}_Q/V_a + \dot{K}_R/V_a$, after dividing both sides by V_a, and we arrive at the following charge-based current continuity equation:

$$I = I_L + I_Q + I_R, \tag{5}$$

where I_L and I_Q are the capacitive contributions to the currents, which come from the non-dissipative electrostatic potential energies, whereas I_R is a resistive current. Therefore, the above charge-based current continuity relation can be represented as a parallel circuit composed of two capacitors C_L and C_Q, and one resistor R_Q, as shown in Fig. 1c.

Transformation to an electric-field-based circuit. The currents I_L and I_Q are transformed from K_L and K_Q, respectively. To understand the current continuity in terms of the electric field, K_L and K_Q should be transformed from the charge-based electrostatic potential energies to the electric-field-based currents. As we have already shown, K_Q is transformed using the current relation $I_Q = I_{EE} + I_{VE}$. In addition, K_L can be transformed into the electric field energy. If we assume the surface of the emitter is a Gaussian surface, Gauss's law for the emitter charge Q_L can be written as $\int_{Se} \mathrm{ELp} \cdot d\mathbf{s}' = Q_L/\varepsilon$ when there is no space-charge; here $\mathbf{E}_{Lp}$ is the Laplacian electric field and $\mathbf{s}'$ is the vector area ($\mathbf{s}' = -\mathbf{s}$, see Fig. 1a). This relation however applies even in the presence of space-charge, since Q_L is not influenced by the space-charge, as discussed previously. By substituting the expression $Q_L = \varepsilon \int_{Se} \mathbf{E}_{Lp} \cdot d\mathbf{s}'$ into $K_L = 1/2 Q_L V_a$, we obtain $K_L = K'_{VE}\left(=1/2\varepsilon \int_{Se} V_a \mathbf{E}_{Lp} \cdot d\mathbf{s}'\right)$, as well as $I_L = I'_{VE}$ by employing the transformation rule. By inserting $I_Q = I_{EE} + I_{VE}$ and $I_L = I'_{VE}$ into equation (5), we obtain $I = I'_{VE} + I_{EE} + I_{VE} + I_R$. Consequently, if I'_{VE} and I_{VE} are combined into an equivalent current $I_S(=I_{VE} + I'_{VE})$, we arrive at the following electric-field-based current continuity:

$$I = I_{EE} + I_S + I_R, \tag{6}$$

where I_S given by

$$I_S = \frac{1}{V_a}\frac{d}{dt}\left(\frac{1}{2}\varepsilon \int_{Se} V_a\left(\mathbf{E} - \mathbf{E}_{Lp}\right) \cdot d\mathbf{s}\right). \tag{7}$$

The term I_{EE} in equation (6) is the non-dissipative volumetric current, and includes a volume integral (see K_{EE} in equation (1)), whereas I_S in equation (7) is a non-dissipative surficial current which includes the surface integral. The volumetric current I_{EE} and surficial current I_S are geometrically independent. Hence, the above electric-field-based current continuity relation can be represented as a parallel circuit composed of two capacitors C_{EE} and C_S, and one resistor R_Q, as shown in Fig. 1d.

Validation. An experimental setup consisting of an axisymmetric wire-to-cylinder positive air corona discharge[28] was used to validate the theoretical framework described here, as shown in Fig. 2a (see Methods for details of the experiment). If a positive voltage applied to the emitter exceeds the corona discharge initiation voltage, a positive charge (i.e., a collection of positive ions) will be generated in a thin plasma sheath around the emitter[28,29] (shown by the dotted circle in Fig. 2a), and that charge will drift toward the collector due to the Coulomb force[28,29]. Here we assume that the applied bias is described by a sinusoidal waveform with a DC offset, as shown in the leftmost two waveforms in Fig. 2b, i.e., $V_a = V_m + V_o \sin(2\pi f)t$, where V_m is the mean voltage (i.e., DC offset), V_o is the amplitude of the time-varying component, f is the frequency of the time varying component (so that $T = 1/f$ is the period), and t is time. The purpose of this waveform is to enable time-varying motion of the space-charge.

First, we attempt to reproduce the parallel topology discussed above. The terms C_L and C_Q (see Fig. 1c) result from K_L (due to the electrodes) and K_Q (due to the space-charge), whereas C_{EE} and C_S (see Fig. 1d) result from K_{EE} (for the volume) and K_S (for the surface). The summation of these geometrically separated energies corresponds to the parallel connection of two capacitors. However, concerning the space-charge, it is not clear whether the drift of the point charge ΔQ (see Fig. 1a) corresponds to a parallel or series connection of $C_{\Delta Q}$ and $R_{\Delta Q}$. In this respect, it is helpful to experimentally confirm the parallel connection between R_Q and the two capacitances. With periodic conditions, the mean circuit

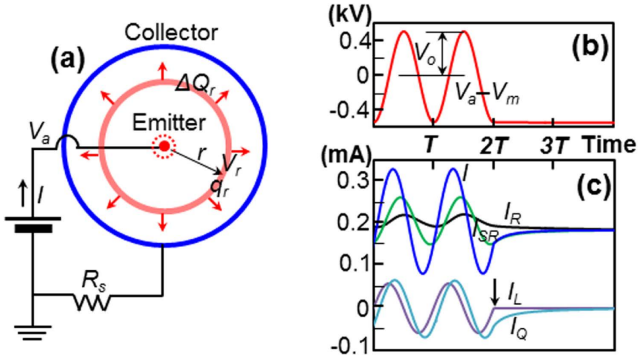

Figure 2. Experimental setup and simulated currents. (**a**) A schematic diagram showing the wire-to-cylinder positive air corona discharge. The outer radius of the emitter was $r_e = 0.02$ mm, the inner radius of the collector was $r_c = 17$ mm, and the length (perpendicular depth of cross-section) was $l = 100$ mm. The theoretical value of C_L is given by $2\pi\varepsilon l/\ln(r_c/r_e) = 0.825$ pF, where ε is the permittivity of free space and R_S is the shunt resistance. The eight radial arrows show the axisymmetric drift of annular discrete charge ΔQ_r at radius r. V_r is the electric potential at r and q_r is the charge density at r. The dotted circle shows the boundary of the plasma sheath with the radius $r_p \approx 3r_e$(see Methods). (**b**) The waveform of applied voltage used for experiments and simulation (the left half shows $t \leq 2T$), where $V_m = 9$ kV, $V_o = 0.53$ kV, $f = 20$ kHz and $T = 50\,\mu$s. (**c**) Transition of the simulated currents from time-varying to the steady-state. The current I is shown in blue, I_{SR} in green, and $I_L = 0$ is shown by the symbol $\downarrow$. The left-hand side corresponds to the loop V_a-I (see Fig. 4a).

current $I_{mean}\left(=T^{-1}\int_0^T Idt\right)$ of the proposed parallel circuit should always be equal to the mean resistor current for a given V_m because the mean of the capacitor current is zero regardless of frequency. For $V_m = 9$ kV, as shown in Fig. 3a, the experimental result reveals that the V_a-I loop contracted to the line A as the frequency decreased from 20 kHz to 1 kHz. Consequently, I_{mean} for each axisymmetric current loop exactly coincides with one centred point for all frequencies, which corresponds to a parallel circuit topology. Figure 3b provides further support of this when V_m and V_o are varied. The solid line in Fig. 3b shows the DC current-voltage curve, which is the same as the V_m-I_{mean} curve for $f = 0$ kHz. For $f = 20$ kHz and $V_o = 1.0$ kV, the centred point coincides exactly with the V_m-I_{mean} curve at the three points of V_m, and with $f = 100$ kHz and $V_o = 0.1$ kV, the centred point coincides exactly with the V_m-I_{mean} curve at the five points of V_m.

To quantitatively understand the theoretical framework described above, the Poisson and charge conservation equations were solved for the experimental setup to obtain the time-varying equivalent currents and circuit components (see Methods for details of the simulation). Note that the electrode current I_L was calculated from $K_L = 1/2C_L V_a^2$ using the theoretical value of C_L (0.825 pF, see Fig. 2a). Figure 4a shows various current-voltage loops for $f = 20$ kHz, which are plotted for the fully periodic state. In the lower part of the figure, the loop I_Q coincides with the loop $I_{EE} + I_{VE}$, whereas the loop I_L coincides with the loop I'_{VE}. This supports the relations $I_Q = I_{EE} + I_{VE}$ and $I_L = I'_{VE}$, which are pivotal in the charge-to-field transformation. In addition, the surficial current I_S is revealed to be a considerable loop. The complete coincidence of the loop I (i.e., the sum of I_L, I_Q and I_R) and the loop I_t (the sum of I_{EE}, I_S and I_R) supports the equivalence of charge-based and electric-field-based approaches.

Figure 4b shows a comparison between the measured circuit current I and the simulated current for the case shown in Fig. 4a. Although the two loops are in very good agreement, both in terms of the overall shape and the instantaneous data, a small discrepancy was observed at the top. The experimentally measured loop was somewhat distorted, compared with the simulated data, which is attributed to the incomplete sine wave generated by the power supply, and the measured capacitance $C_L = 0.89$ pF was found to provide better agreement. As shown in Fig. 4c, similar agreement was achieved with $f = 100$ kHz, which supports our theoretical result; i.e., the two equivalent circuits shown in Fig. 1.

Comparison with the Shockley-Ramo theorem. This theorem expresses the circuit current induced by the point space-charge ΔQ as $\Delta Q\mathbf{U}_{\Delta Q} \cdot \mathbf{E}_{Lp}$ for an applied bias of 1 V, which leads to the relation $I_{SR} = V_a^{-1}\int_v q\mathbf{U} \cdot \mathbf{E}_{Lp} dv$ [30] for the total space-charge. When we plot I_{SR}, as shown in Fig. 4b,c the results were in poor agreement with the experimentally measured current for both cases. It has been reported[1,13,31] that the electrode current I_L should be added to I_{SR} to provide the correct external circuit current, since I_{SR} is obtained with a fixed V_a. This appears reasonable for a time-varying V_a; however, as shown in Fig. 4b,c, $I_L + I_{SR}$ did not provide good agreement with the experimentally measured current. Figure 2c shows the transition of the current from the time-varying applied bias to the steady-state. The

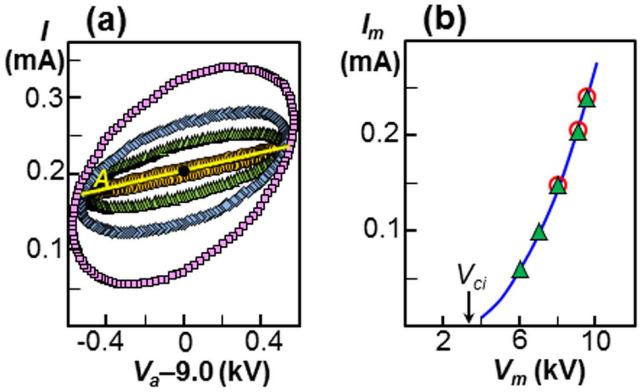

Figure 3. Experimental validation of the parallel circuit topology. (**a**) V_a-I loops for frequencies of 20 kHz (□), 10 kHz (◇) 5 kHz (△) and 1 kHz (○). The coincidences of I_{mean}(●) were as follows: 0.206 mA for 0.2 kHz, 0.207 mA for 0.5 kHz, 0.206 mA for 1 kHz, 0.204 mA for 2 kHz, 0.207 mA for 5 kHz, 0.204 mA for 10 kHz and 0.204 mA for 20 kHz, average: 0.2054 mA, standard deviation: 0.0013 mA. The 2-kHz loop is plotted between 1- and 5-kHz loops (not shown). The 0.2-kHz and 0.5-kHz loops were almost identical to line *A*. (**b**) The experimental DC current-voltage curve reveals typical wire-to-cylinder corona discharge, and can be fitted with $I = 0.00405\ V_a(V_a - V_{ci})$, where $V_{ci} = 3.4$ kV is the corona discharge initiation voltage[28]. Data for $f = 20$ kHz and $V_o = 1.0$ kV are shown by the '○' symbols and data for $f = 100$ kHz and $V_o = 0.1$ kV by the '▲' symbols. Difference between DC data and 8 symbols; average: 0.00042 mA, standard deviation: 0.0012 mA.

current I merged with I_{SR} as V_a became constant, and finally coincided with I_R in the steady state as I_Q became zero. This result suggests that I_{SR} does not predict the circuit current for the motion of space-charge when the applied voltage varies with time.

Comparison with spatial electric currents. The currents shown in the charge-based and electric-field-based current continuities are the equivalent circuit currents, rather than actual currents that flow in the space between two electrodes. Here we compare the equivalent circuit currents with the spatial current density $\mathbf{J}$ that appears in Ampère-Maxwell equation[26], i.e., $\nabla \times \mathbf{H} = \mathbf{J}$, where $\mathbf{H}$ is the magnetic field, and $\mathbf{J} = \mathbf{J}_f + \mathbf{J}_d$, where $\mathbf{J}_f\ (= q\mathrm{U})$ is the conduction current density of free charge and $\mathbf{J}_d\ (= \varepsilon \partial \mathbf{E}/\partial t)$ is the displacement current density. To understand how $\mathbf{J}$ relates to the circuit current, we attempt to visualise the spatial $\mathbf{J}_f$ and $\mathbf{J}_d$ at a moment, which corresponds to the symbols ▲, ● and ■ shown in Fig. 4a. Figure 4d shows the radial distributions of the free charge current $I_f\ (= \int_{Sr} \mathbf{J}_f \cdot d\mathbf{s}$, where *Sr* is surface at radius *r*; see Fig. 2a,) and displacement current $I_d \left(= \int_{Sr} \mathbf{J}_d \cdot d\mathbf{s}\right)$. The ripples that appear in I_f and I_d are due to fluctuations in the applied voltage. Although the shape of $I_{fd}\ (= I_f + I_d)$ appears to be flat with low ripples because the fluctuations of I_f and I_d cancel, those ripples exhibit a wave pattern, as shown by the magnified plot in Fig. 4e. Let $\overline{I}_{fd}$ be the volume average of I_{fd}; although, we find agreement between $\overline{I}_{fd}$ (0.281 mA) and $I_R + I_{EE}$ (0.282 mA), this does not imply an exact equivalence of $\overline{I}_{fd}$ and $I_R + I_{EE}$, and rather suggests that the $\mathbf{J}$ is linked to the volumetric terms $I_R + I_{EE}$. Subsequently, the agreement between I (0.319 mA) and $\overline{I}_{fd} + I_S$ (0.318 mA, where $I_S = 0.037$ mA) supports our theoretical identification of surficial current I_S. Figure 4a shows further overall agreement between $\overline{I}_{fd}$ and $I_R + I_{EE}$ for the entire loop.

The numerically demonstrated link between the spatially averaged $\overline{I}_{fd}$ and the volumetric $I_R + I_{EE}$ is supported theoretically. The term $\dot{K}_R$ can be re-written as $\int_v q\mathbf{E} \cdot \mathbf{U} dv$, whereas K_{EE} in equation (1) is differentiated to give $\dot{K}_{EE} = \int_v \mathbf{E} \cdot \varepsilon (\partial \mathbf{E}/\partial t)\, dv$. Consequently, $\dot{K}_R + \dot{K}_{EE}$ leads to $V_a(I_R + I_{EE}) = \int_v \mathbf{E} \cdot \left(\mathbf{J}_f + \mathbf{J}_d\right) dv$. If we resort to the definition of work rate $\mathbf{E} \cdot \mathbf{J}_f$[26], which is done by the moving charge, the above relation suggests that $\mathbf{J}_f$ is linked to I_R and $\mathbf{J}_d$ is linked to I_{EE}.

Evaluation of circuit components. There are five circuit components: C_L, C_Q, R_Q, C_{EE} and C_S in the two proposed circuits. With the exception of C_L, the other four components can be calculated from the acquired V and q fields. The resistance R_Q can be calculated using equation (3), whereas three capacitances are calculated using equation (2); we arrive at the following expressions: $R_Q = {V_a}^2 / \int_v \mathbf{F} \cdot \mathbf{U} dv$, $C_Q = {V_a}^{-2} \int_v qV dv$, $C_{EE} = {V_a}^{-2} \varepsilon \int_v E^2 dv$ and $C_S = {V_a}^{-2} \varepsilon \int_{S_e} V_a \left(\mathbf{E} - \mathbf{E}_{Lp}\right) d\mathbf{s}$. With the same conditions as the data shown in Fig. 4a, the four components are plotted in Fig. 5a–d. Interestingly, R_Q

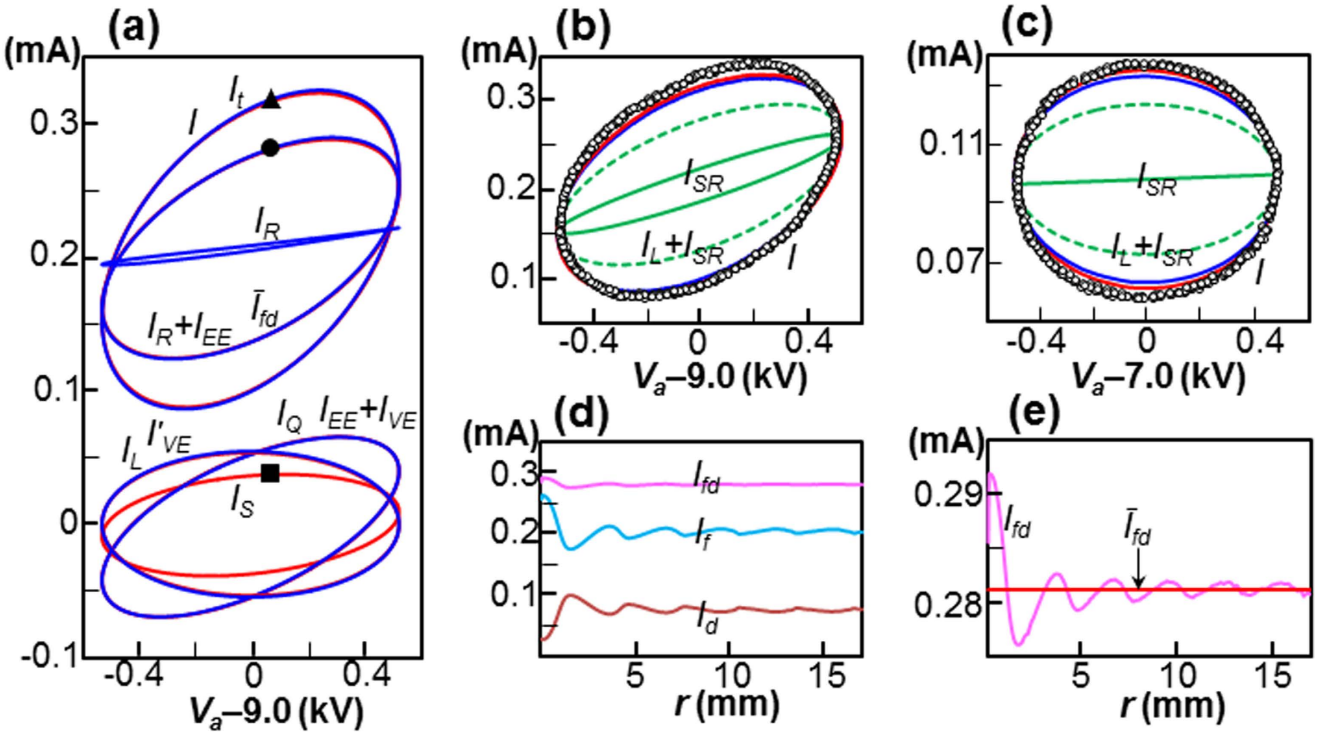

Figure 4. Validation of the theoretical work. (**a**) Simulated V_a-I loops for $f = 20$ kHz, $V_m = 9.0$ kV and $V_o = 0.53$ kV. The components of the current I, I_R, $I_R + I_{EE}$, I_L and I_Q are shown in blue, and I_t, $\bar{I}_{fd}$, I'_{VE}, $I_{EE} + I_{VE}$ and I_S are shown in red. The coincidences between I and I_t, $I_R + I_{EE}$ and $\bar{I}_{fd}$, I_L and I'_{VE}, I_Q and $I_{EE} + I_{VE}$ were so good that the differences cannot be distinguished. ▲: I(0.319 mA), ●: $I_R + I_{EE}$ (0.282 mA), ■: I_S(0.037 mA). (**b**) Circuit current comparison between experiment (○) and simulation (shown by the blue inner loop) for the same conditions as Fig. 4a. The measured capacitance ($C_L = 0.89$ pF) is shown by the red outer loop. The current I_{SR} is shown by the solid green curve, and $I_L + I_{SR}$ is shown by the dashed green curve. (**c**) Additional comparison between experiment (○) and simulation for $f = 100$ kHz, $V_m = 7.0$ kV and $V_o = 0.05$ kV. The current I_{SR} is shown by the solid green curve, and $I_L + I_{SR}$ is shown by the dashed green curve. (**d**) Instantaneous profiles of I_f and I_d plotted with as a function of the radius for $r_e \leq r \leq r_c$. (**e**) A magnified profile of I_{fd} shown in (**d**).

was not fixed. This quantity forms a pinched loop that relates to the time-varying characteristics of the circuit in a similar manner to a memristor R_m[32], and is identical to R_Q from the definition of $V_a = I_R R_m$. The three capacitances C_Q, C_{EE} and C_S lead to three elliptical loops that describe the time-varying characteristics of the system. All of the capacitances, including C_L, are compared in Fig. 5e. The two parallel charge-based and electric-field-based circuits shown in Fig. 1 are equivalent, so that $C_L + C_Q$ should be equal to $C_{EE} + C_S$. The data plotted in Fig. 5e reveal a complete coincidence between $C_L + C_Q$ and $C_{EE} + C_S$. The data plotted in Fig. 5e show that this is indeed the case. This agreement confirms the effectiveness of the proposed method to define the capacitance, which can be extended to the electric field energy.

Capacitive current and time-varying capacitance. We examine the current flowing in the time-varying capacitance C_Q, as shown in Fig. 5b. The time-varying capacitance (which is similar to a memcapacitor[19,32,33]) is defined as $Q = C_Q V_a$, where the capacitor current I_{QA} is defined by applying the product rule for differentiation to $I_{QA} = dQ/dt = d(C_Q V_a)/dt$[32]; i.e.,

$$I_{QA} = V_a \frac{dC_Q}{dt} + C_Q \frac{dV_a}{dt}. \tag{8}$$

The capacitor current I_{QB}, which results from the energy equivalence of $K_Q = 1/2 C_Q {V_a}^2$, can be expressed by applying the product rule to $V_a I_{QB} = \dot{K}_Q = d\,(1/2 C_Q {V_a}^2)/dt$; i.e.,

$$I_{QB} = \frac{1}{2} V_a \frac{dC_Q}{dt} + C_Q \frac{dV_a}{dt}, \tag{9}$$

where I_{QA} and I_{QB} reveal an apparent difference in the first term, which reflects the effects of the unsteady capacitance; i.e., $V_a(dC_Q/dt)$ for I_{QA}, and $1/2 V_a(dC_Q/dt)$ for I_{QB}. It should be noted, however, that both I_{QA}

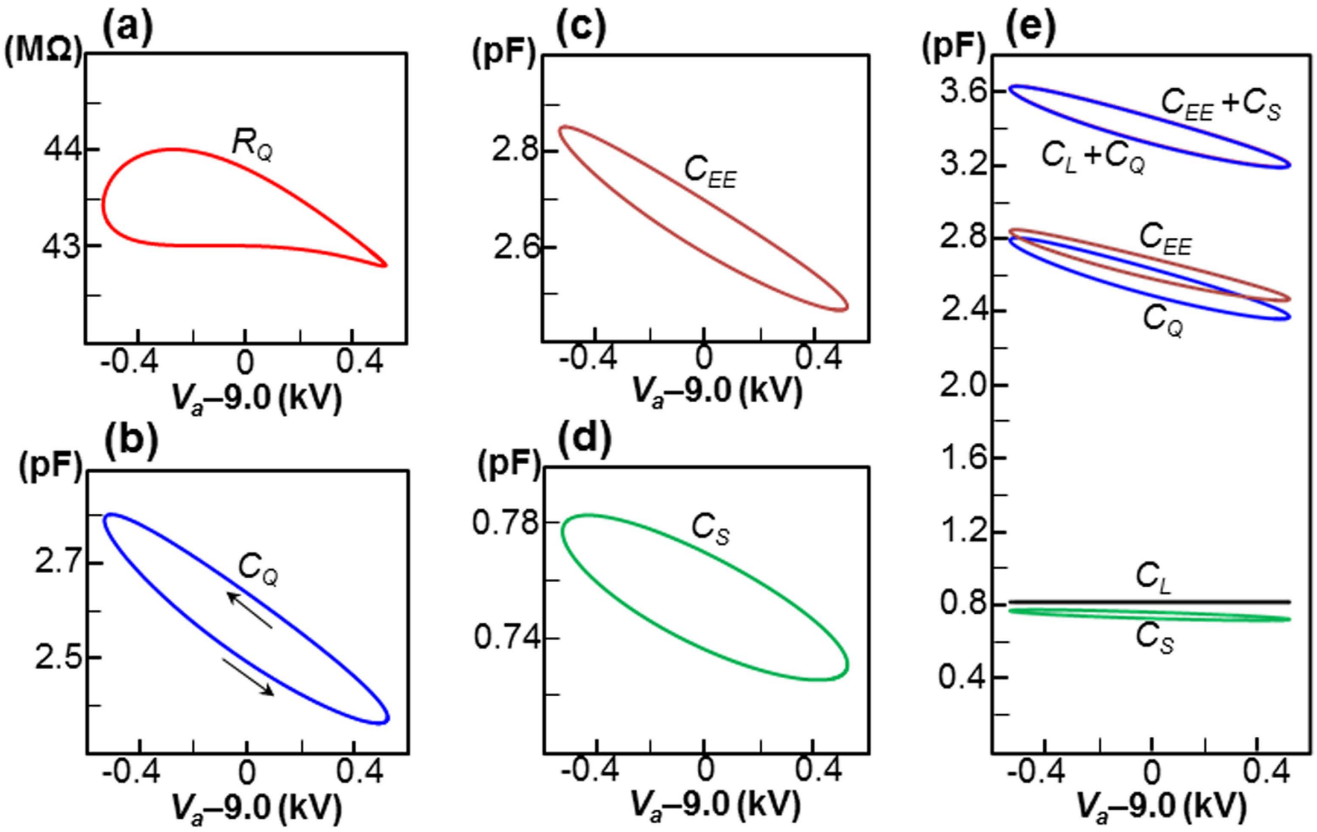

Figure 5. Evaluation of time-varying circuit components at 20 kHz. (**a**) V_a-R_Q. (**b**) V_a-C_Q. The direction of the two arrows agrees with the time increment. (**c**) V_a-C_{EE}. (**d**) V_a-C_S. (**e**) All capacitances are compared. The $C_L + C_Q$ loop (blue) coincides with $C_{EE} + C_S$ loop (red) such that the difference is barely distinguishable.

and I_{QB} reduce to the usual capacitor current relation of $I_Q = C_Q(dV_a/dt)$ when C_Q is constant. Figure 6a shows a comparison between I_{QA} and I_{QB} for $f = 20$ kHz. The exact coincidence of I_{QB} with I_Q, which is calculated from $K_Q = 1/2\int_v qVdv$, suggests that equation (9) is more plausible than equation (8) to describe the time-varying capacitance.

Figure 5e shows that the electrode capacitance C_L is approximately one third of C_Q. It follows that I_L should be one third of I_Q, according to the usual capacitor current relation; however, the I_Q and I_L loops plotted in Fig. 4a have approximately same magnitude at the point $V_a \approx 9$ kV. This apparent contradiction can be resolved by considering the effect of the time-varying capacitance. In Fig. 6b, the quantity I_{QB} that is plotted in Fig. 6a is decomposed into that due to the time-varying capacitance, which is denoted I_{QB1} ($= 1/2V_a(dC_Q/dt)$), and that due to the steady-state capacitance, denoted I_{QB2} ($= C_Q(dV_a/dt)$), where $I_{QB} = I_{QB1} + I_{QB2}$. With $V_a \approx 9$ kV, the relatively large value of I_{QB2} (0.165 mA) was counterbalanced by the negative value of I_{QB1} (−0.113 mA) to create a relatively small value of I_{QB} (0.053 mA). This counterbalancing effect of the time-varying capacitance is sufficiently large ($I_{QB1}/I_{QB2} = -0.68 \approx -2/3$) to allow I_{QB} to be one third of the usual capacitor current I_{QB2}. With $f = 100$ kHz, as shown in Fig. 6c, a similar counterbalancing effect was observed at the point $V_a \approx 7$ kV; i.e., $I_{QB2} = 0.066$ mA, $I_{QB1} = -0.044$ mA and $I_{QB} = 0.022$ mA, so that we have $I_{QB1}/I_{QB2} = -0.67$. As shown in Fig. 6d, the I_{QB2}-I_{QB1} relations form elliptical loops, with a narrow outer loop for $f = 20$ kHz and a thin inner loop for $f = 100$ kHz. These two points correspond to the bottom-right corners of the two loops. The lower turning point shown in Fig. 6d corresponds to the arrow to the right (→) in Fig. 6b and the lower arrow (↘) of Fig. 5b. This tilted arrow corresponds to an increase in V_a ($dV_a/dt > 0$) and decrease in C_Q ($dC_Q/dt < 0$), which leads to a positive I_{QB2} and a negative I_{QB1} at the lower turning point of Fig. 6d. In the same manner, the upper turning point shown in Fig. 6d corresponds with the upper arrow (↖) of Fig. 5b. This tilted arrow corresponds to a decrease in V_a ($dV_a/dt < 0$) and an increase in C_Q ($dC_Q/dt > 0$), which gives a negative I_{QB2} and a positive I_{QB1} in the upper turning point of Fig. 6d.

The terms I_{QB2} and I_{QB1} exhibit a phase difference of 180° in the time domain (see Fig. 6b,c). This can be interpreted as follows: I_{QB1} behaves as an inductor current rather than the usual capacitor current I_{QB2}. The overall linear relation between I_{QB1} and I_{QB2} shown in Fig. 6d is $I_{QB1} \approx -0.7I_{QB2}$ at both 20 kHz and 100 kHz, where the –0.7 implies a significant counterbalancing effect of the rate of change of the

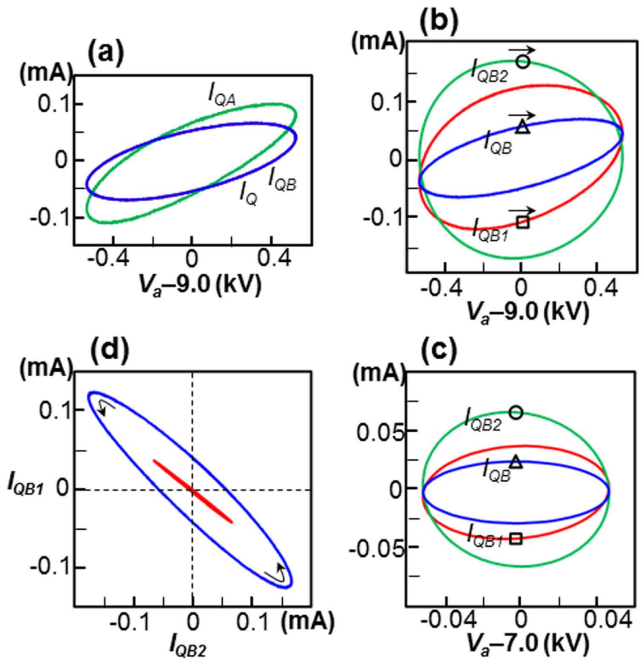

Figure 6. Analysis of capacitive current due to space-charge. (**a**) Comparison between I_{QA} and I_{QB} for 20 kHz (see Fig. 4a). The I_Q loop (blue) coincides with the I_{QB} loop (red) such that the difference is not clearly distinguishable. (**b**) The quantity I_{QB} (△ symbol) plotted in Fig. 6a is decomposed into I_{QB1} (□ symbol) and I_{QB2} (○ symbol). The directions of the three arrows agree with the time increment. (**c**) The I_{QB} (△ symbol) is decomposed into I_{QB1} (□ symbol) and I_{QB2} (○ symbol) for $f = 100$ kHz (see Fig. 4c). (**d**) I_{QB1} and I_{QB2} relations; the outer loop (blue) corresponds to $f = 20$ kHz and the thin inner loop (red) to $f = 100$ kHz. The direction of the two arrows agrees with the time increment.

capacitance with the time-varying motion of the space-charge. This relation will hold only for the completely periodic case under the DC biased sinusoidal waveform of applied voltage adopted in this report.

Discussion

Our analysis is restricted to the electrostatic potential energy of positive space-charge; however, the approach can also be applied to negative space-charge. Considering the symmetry of positive and negative charges, the reference of electric potential for the negative space-charge should be changed from collector to emitter in Fig. 1a. In this case, the electric potential energy of the discrete negative charge $-\Delta Q$ located in the local electric potential $V_{\Delta Q}$ is expressed as the positive value of $K_{\Delta Q} = 1/2(-\Delta Q)(V_{\Delta Q} - V_a)$.

Regarding the method used to define the capacitance, we reconsider the usual definition of $Q_L = C_L V_a$ for the application to space-charge. According to this definition, the capacitance due to space-charge ΔQ can be deduced from $\Delta Q = \hat{C}_{\Delta Q} V_{\Delta Q}$, where $\hat{C}_{\Delta Q}$ is the local capacitance for the local $V_{\Delta Q}$. The $\Delta Q = \hat{C}_{\Delta Q} V_{\Delta Q}$ is identical to the proposed definition of $K_{\Delta Q} = 1/2\hat{C}_{\Delta Q} {V_{\Delta Q}}^2$ if $K_{\Delta Q} = 1/2\Delta Q V_{\Delta Q}$; however, $\hat{C}_{\Delta Q}$ should be transformed to the circuit capacitance $C_{\Delta Q}$, which is defined at the circuital V_a. We employ the energy equivalence relation $K_{\Delta Q} = 1/2\hat{C}_{\Delta Q} {V_{\Delta Q}}^2 = 1/2 C_{\Delta Q} {V_a}^2$ for this transformation. It follows that this transformation rule can be expressed as $C_{\Delta Q} = \hat{C}_{\Delta Q}(V_{\Delta Q}/V_a)^2$, which supports our definition of the capacitance due to ΔQ in equation (4) when $\Delta Q = \hat{C}_{\Delta Q} V_{\Delta Q}$ is applied. In other words, our proposed method to define the capacitance can be said to be the capacitance transformation from one voltage to another, without violating the conventional method.

The physical interpretation of the two charge-based and electric-field-based current continuities is discussed using three examples. For the time-varying case with no space-charge, the Ohmic current I_R due to the drift of space-charge disappears, and the surficial current I_S becomes zero from $\mathbf{E} = \mathbf{E}_{Lp}$ (see equation (7)). It follows that the electric-field-based current continuity reduces to $I = I_{EE}$, whereas charge-based continuity reduces to $I = I_L$, since both I_Q and I_R are zero. The following relation $I_L = I_{EE}$ can be transformed to a $K_L = K_{EE}$ relation, which implies a textbook example[26]; i.e., the electrostatic potential energy stored in the electrode capacitor is equal to the volumetric electric field energy between the electrodes. In this case, the displacement current I_d is equal to the circuit current I[26]. For the steady state case with space-charge, both current continuities result in $I = I_R$, which is an example of steady-state electrical

discharge[27,29,34]. In this case, the motion of free charges, and the corresponding current I_f is equal to the circuit current I. With the time-varying case, however, as shown in Fig. 4a, the average spatial current $\overline{I}_{fd}$ is lower than the circuit current by an amount I_S. From the perspective of field theory, the surface integral K_{VE} in equation (1) is considered to be negligible compared with the volume integral K_{EE}, by assuming a very large enclosed volume[26]. It follows that all of the electric field energy can be considered to be stored only in the spatial electric field[26]. However, K_{VE} was not neglected in the configuration discussed here because of the small enclosed volume. In this context, a so-called surficial current I_S may be taken as an additional spatial current.

The circuital characteristics of the motion of the space-charge with a time-varying applied bias can be summarised as follows. The microscopic behaviour of the space-charge is decomposed to a discrete equivalent circuit resistance and a discrete equivalent circuit capacitance. These microscopic components evolve in parallel with the macroscopic equivalent circuit components to form a charge-based circuit, which can be equivalently transformed into an electric-field-based circuit. All of the circuit components calculated using the space-charge and electric-potential fields vary with time, in accordance with the time-varying motion of the space-charge. With the configuration discussed here, 70% of the usual capacitive current was significantly counterbalanced by the current due to the rate of change of the capacitance. The two approaches were crucial for the theoretical framework described here: the transformation rule, which was used to transform electrical energy into an equivalent circuit current, and the method to define the capacitance, which is based on energy equivalence. The Shockley-Ramo theorem was shown to be invalid when the applied voltage was time-varying. The electric-field-based current continuity description includes an additional electric current to describe the oscillatory motion of the space-charge. We expect that our results and approach will be helpful for understanding experimental results, the design of equivalent circuits, and further theoretical studies in relevant fields.

Methods

Experiment. Figure 2a shows a cross-section of the wire-to-cylinder air corona discharge configuration with a central emitter formed of tungsten wire, with a diameter of 40 μm, inside a circular collector, which was formed of stainless steel pipe, with an inner diameter of 34 mm. This experimental configuration was used to approximate the one-dimensional electric potential and charge density distributions, by eliminating any edge effects. For the collector structure, five small cylindrical stainless steel tubes that were 100 mm long were assembled to form a long pipe, where for each pipe the neighbouring pipes were electrically insulated by a small air gap. The tungsten wire was placed under tension and carefully centred along the axis inside the pipes. The five collector pipes were then electrically connected in parallel, and a shunt resistance of $R_S = 10\,\mathrm{k}\Omega$ (see Fig. 2a) was connected to each pipe in series to measure the current. A preliminary experiment was carried out to evaluate the experimental electrode capacitance C_L of each pipe without space-charge (i.e., with $V_a < V_{ci}$, see Fig. 3b). When C_L was calculated using $V_{a,rms} = I_{rms}/(\omega C_L)$, where $\omega = 2\pi f$ and the subscript *rms* stands for root-mean-square, the central pipe exhibited the smallest capacitance (0.89 pF), which corresponds to the measured C_L. The phase difference θ between V_a and I was observed to change as the frequency was varied; we find $\theta = 84.2°$ for $f = 20$ kHz, and $\theta = 65.0°$ for $f = 100$ kHz, in contrast to the expected value of $\theta = 90°$. Furthermore, the capacitance was observed to be independent of the frequency. Positive discharge exhibited a more stable current waveform than negative discharge. Mechanical vibration of the wire was minimised by fixing the wire with small pieces of dielectric (thin pieces of paper) inserted through the four gaps between neighbouring pairs of pipes. In the experiments, the current in the central pipe was measured for positive corona discharge with phase compensation of 5.8° for $f = 20$ kHz (see Fig. 4b) and 25.0° for $f = 100$ kHz (see Fig. 4c).

The waveform V_a was generated using a high-voltage amplifier (10/40A, TREK) triggered by a function generator (WF1974, NF). V_a was measured using a 1000:1 divider inside the 10/40A amplifier. The circuit current I was calculated using Ohm's law from the measured voltage drop across the shunt resistance R_s. The waveforms of V_a and I were observed using a storage oscilloscope (6050A, LeCroy), and the stored data were processed to obtain the experimental data. The experiments were carried out with a temperature in the range 27.8-28.1 °C and a relative humidity in the range 51.0-52.2%.

Simulation. We solved the Poisson's equation (i.e., $\nabla^2 V = -q/\varepsilon$) coupled with the charge conservation equation $\partial q/\partial t + \nabla \cdot \mathbf{J}_f = 0$ for the space between r_e and r_c, corresponding to the experimental arrangement. The Laplace equation $\nabla^2 V = 0$ was also solved to obtain the electric field $\mathbf{E}_{Lp}$, which is necessary to calculate I_S and I_{SR}. The term $\mathbf{J}_f$ in the charge conservation equation is given by $\mathbf{J}_f = q(\mathbf{U}_c + \mathbf{U}) - D\nabla q$, where $\mathbf{U}_c$ is the convective fluid velocity, $\mathbf{U}(= \mu\mathbf{E})$ is the velocity of the charge (i.e., ion), μ is the mobility of the ion, and D is the diffusion coefficient[29]. The effects of $\mathbf{U}_c$ and diffusion were neglected (i.e., we assumed $\mathbf{U}_c = 0$ and $D = 0$)[29]. We used a value of $\mu = 1.4 \times 10^{-4}\,\mathrm{m^2V^{-1}s^{-1}}$ for the mobility of the positive ions[35,36]. The permittivity of free space was used for ε[29].

We followed the simulation method that we have previously reported for steady-state simulations[27,29,34]. To achieve the precise time-varying simulation required for this study, we took advantage of the symmetry of the system, so that the equations could be solved in one dimension, which provides significant gains in terms of the computational expense. V_r and q_r (see Fig. 2a) are functions of the radius and time. The grid structure was composed of one string of 236 cells with dense grids on the emitter side (start size:

2 μm, growth rate: 1.05, maximum size: 100 μm) to describe the large gradient of V_r and q_r near the emitter. The time-step was 0.2 ns, which maintains a maximum Courant number (charge velocity × iteration time/cell size) of $Cr < 0.1$ in the first cell above the surface of the emitter. Dirichlet boundary conditions were used for V_r at the emitter ($V_r = V_a$) and the collector ($V_r = 0$), and we imposed $\partial q_r/\partial r = 0$ at both electrodes. A "constant charge density" (q_i) model was used to represent the charge generation process in the plasma region around the emitter with the assumption that the radius of the plasma sheath is given by $r_p \approx 3r_e$[29] (see the dotted circle in Fig. 2a). As the first step in the q_i decision process, we measured the DC current I for a given V_a. The steady-state simulation subsequently followed to make the simulated current (i.e., integration of $\mathbf{J}_f$ on the collector surface) coincide with the measured I by adjusting q_i of the plasma region, and resulted in $q_i = 0.0191\,\mathrm{Cm}^{-3}$ for $V_m = 9.0$ kV case and $q_i = 0.0038\,\mathrm{Cm}^{-3}$ for $V_m = 7.0$ kV case. We used a V_a waveform with a very small ratio V_o/V_m for the above plasma region model in the time-varying simulation, with a high frequency to increase the influence of capacitive currents I_L and I_Q, i.e., $V_o/V_m = 0.059$ (0.53 kV and 9.0 kV) at 20 kHz and $V_o/V_m = 0.0071$ (0.05 kV and 7.0 kV) at 100 kHz.

From the simulated time-varying V and q fields, we calculated the components of the currents shown in Fig. 4a using $\Delta K_X/\Delta t/V_a$ (where $\Delta t = 40$ ns); $K_Q(=\sum 1/2\,(q\Delta v)\,V) \rightarrow I_Q$, $K_{EE}(=\sum 1/2\varepsilon\,|\mathbf{E}|^2\Delta v) \rightarrow I_{EE}$, $K_{VE}\left(=1/2\varepsilon V_a\,|\mathbf{E}|_{Se}\,(-Se_A)\right) \rightarrow I_{VE}$, $K_L(=1/2C_L{V_a}^2) \rightarrow I_L$, $K'_{VE}\left(=1/2\varepsilon V_a\left|\mathbf{E}_{Lp}\right|_{Se} Se_A\right) \rightarrow I'_{VE}$, $K_S(=K_{VE} + K'_{VE}) \rightarrow I_S$ and $\dot{K}_R(=\sum(q\Delta v)\,|\mathbf{E}| \cdot \mu|\mathbf{E}|) \rightarrow I_R$, where Δv is the volume of each cell, and Se_A is the area of the surface of the emitter. The circuit components shown in Fig. 5 were calculated using $R_Q = {V_a}^2/(\sum(q\Delta v)\,|\mathbf{E}| \cdot \mu|\mathbf{E}|)$, $C_Q = \sum(q\Delta v)\,V/{V_a}^2$, $C_{EE} = \varepsilon\sum|\mathbf{E}|^2\Delta v/{V_a}^2$ and $C_H = \varepsilon\sum V_a\left(\left|\mathbf{E}_{Lp}\right|_{Se} - |\mathbf{E}|_{Se}\right)Se_A/{V_a}^2$.

References

1. Shockley, W. Currents to conductors induced by a moving point charge. *J. Appl. Phys.* **9,** 635–636 (1938).
2. Ramo, S. Currents induced by electron motion. *Proc. I.R.E* **27,** 584–585 (1939).
3. Nonner, W., Peyser, A., Gillespie, D. & Eisenberg, B. Relating microscopic charge movement to macroscopic currents: the Ramo-Shockley theorem applied to ion channels. *Biophys. J* **87,** 3716–3722 (2004).
4. Millar, C., Asenov, A. & Roy, S. Self-consistent particle simulation of ion channels. *J. Comput. Theor. Nanosci.* **2,** 1–12 (2005).
5. Eisenberg, B. & Nonner, W. Shockley-Ramo theorem measures conformation changes of ion channels and proteins. *J. Comput. Electron* **6,** 363–365 (2007).
6. Reklaitis, A. Monte Carlo study of dc and ac vertical electron transport in a single-barrier heterostructure. *Phys. Rev. B* **63,** 155301 (2001).
7. Shiktorov, P. *et al.* Theoretical investigation of Schottky-barrier diode noise performance in external resonant circuits. *Semicond. Sci. Technol.* **21,** 550–557 (2006).
8. Pavlica, E. & Bratina, G. Displacement current in bottom-contact organic thin-film transistor. *J. Phys. D: Appl. Phys* **41,** 135109 (2008).
9. Marescaux, M., Beunis, F., Strubbe, F., Verboven, B. & Neyts, K. Impact of diffusion layers in strong electrolytes on the transient current. *Phys. Rev. E* **79,** 011502 (2009).
10. Neyts, K. *et al.* Charge transport and current in non-polar liquids. *J. Phys.: Condens. Matter* **22,** 494108 (2010).
11. Morrow, R. The theory of positive glow corona. *J. Phys. D: Appl. Phys.* **30,** 3099–3114 (1997).
12. Naidis, G. V. Modelling of streamer propagation in atmospheric-pressure helium plasma jets. *J. Phys. D: Appl. Phys.* **43,** 402001 (2010).
13. He, Z. Review of the Shockley-Ramo theorem and its application in semiconductor gamma-ray detectors. *Nucl. Instrum. Methods Phys. Res. Sect. A* **463,** 250–267 (2001).
14. Jeong, M. & Hammig, M. D. The atomistic simulation of thermal diffusion and Coulomb drift in semiconductor detectors. *IEEE Trans. Nucl. Sci.* **56,** 1364–1371 (2009).
15. Göök, A., Hambsch, F. -J., Oberstedt, A. & Oberstedt, S. Application of the Shockley-Ramo theorem on the grid inefficiency of Frisch grid ionization chambers. *Nucl. Instrum. Methods Phys. Res. Sect. A* **664,** 289–293 (2012).
16. Pons, J., Moreau, E. & Touchard, G. Asymmetric surface dielectric barrier discharge in air at atmospheric pressure: electrical properties and induced airflow characteristics. *J. Phys. D: Appl. Phys.* **38,** 3635–3642 (2005).
17. Singh, K. P. & Roy, S. Impedance matching for an asymmetric dielectric barrier discharge plasma actuator. *Appl. Phys. Lett.* **91,** 081504 (2007).
18. Kriegseis, J., Grundmann, S. & Tropea, C. Power consumption, discharge capacitance and light emission as measures for thrust production of dielectric barrier discharge plasma actuators. *J. Appl. Phys.* **110,** 013305 (2011).
19. Krems, M., Pershin, Y. V. & Di Ventra, M. Ionic memcapacitive effects in nanopores. *Nano lett.* **10,** 2674–2678 (2010).
20. Albrecht, T. How to understand and interpret current flow in nanopore/electrode devices. *ACS Nano* **5,** 6714–6725 (2011).
21. Balijepalli, A. *et al.* Quantifying short-lived events in multistate ionic current measurements. *ACS Nano* **8,** 1547–1553 (2014).
22. Khanal, D. R. & Wu, J. Gate coupling and charge distribution in nanowire field effect transistors. *Nano lett.* **7,** 2778–2783 (2007).
23. Salahuddin, S. R. & Datta, S. Use of negative capacitance to provide voltage amplification for low power nanoscale devices. *Nano lett.* **8,** 405–410 (2008).
24. Knopfmacher, O. *et al.* Nernst limit in dual-gated Si-nanowire FET sensors. *Nano lett.* **10,** 2268–2274 (2010).
25. Zwolak, M. & Di Ventra, M. Colloquium: Physical approaches to DNA sequencing and detection. *Rev. Mod. Phys.* **80,** 141–165 (2008).
26. Griffiths, D. J. *Introduction to electrodynamics* (Prentice-Hall, New Jersey, 1999).
27. Kim, C. *et al.* Microscopic energy conversion process in the ion drift region of electrohydrodynamic flow. *Appl. Phys. Lett.* **100,** 243906 (2012).
28. Sigmond, R. S. Simple approximate treatment of unipolar space-charge-dominated coronas: the Warburg law and the saturation current. *J. Appl. Phys.* **53,** 891 (1982).
29. Kim, C. & Hwang, J. The effect of charge mode transition on electrohydrodynamic flow in a multistage negative air corona discharge. *J. Phys. D: Appl. Phys.* **45,** 465204 (2012).
30. De Visschere, P. The validity of Ramo's theorem. *Solid-State Electron* **33,** 455–459 (1990).
31. Pellegrini, B. Electric charge motion, induced current, energy balance, and noise. *Phys. Rev. B* **34,** 5921–5924 (1986).

32. Di Ventra, M., Pershin, Y. V. & Chua, L. O. Circuit elements with memory: memristors, memcapacitors, and meminductors. *Proc. IEEE* **97,** 1717–1724 (2009).
33. Wang, D. *et al.* Transmembrane potential across single conical nanopores and resulting memristive and memcapacitive ion transport. *J. Am. Chem. Soc.* **134,** 3651–3654 (2012).
34. Kim, C., Noh, K. C., Kim, S. Y. & Hwang, J. Electric propulsion using an alternating positive/negative corona discharge configuration composed of wire emitters and wire collector arrays in air. *Appl. Phys. Lett.* **99,** 111503 (2011).
35. Hirsikko, A. *et al.* Atmospheric ions and nucleation: a review of observations. *Atmos. Chem. Phys.* **11,** 767–798 (2011).
36. Hinds, W. C. in *Aerosol technology: properties, behavior, and measurement of airborne particles* 2nd edn, Ch 15, p 323 (Wiley-Interscience, 1998).

Acknowledgments

This research was supported by Basic Science Research Program through the National Research Foundation of Korea (NRF) funded by the Ministry of Education (NRF-2013R1A1A2A10058503), Mid-career Researcher Program (#2012-R1A2A2A01005449), National Nuclear R&D Program (#2013-M2B2A9A03051296).

Author Contributions

E.-Y.M. conceived of the research project; C.K. formulated the theoretical framework; J.H. and C.K. contributed to the experiment setup and analytical tools; C.K. and E.-Y.M. carried out the experiments, analysed the data and wrote the manuscript; J.H. and H.H. reviewed the manuscript.

Additional Information

Competing financial interests: The authors declare no competing financial interests.

How to cite this article: Kim, C. *et al.* Circuital characterisation of space-charge motion with a time-varying applied bias. *Sci. Rep.* **5**, 11738; doi: 10.1038/srep11738 (2015).